SCIENTIFIC REPORTS

OPEN

Insights into cerebral haemodynamics and oxygenation utilising *in vivo* mural cell imaging and mathematical modelling

Received: 5 October 2017
Accepted: 16 December 2017
Published online: 22 January 2018

Paul W. Sweeney[1], Simon Walker-Samuel[2] & Rebecca J. Shipley[1]

The neurovascular mechanisms underpinning the local regulation of cerebral blood flow (CBF) and oxygen transport remain elusive. In this study we have combined novel *in vivo* imaging of cortical microvascular and mural cell architecture with mathematical modelling of blood flow and oxygen transport, to provide new insights into CBF regulation that would be inaccessible in a conventional experimental context. Our study indicates that vasoconstriction of smooth muscle actin-covered vessels, rather than pericyte-covered capillaries, induces stable reductions in downstream intravascular capillary and tissue oxygenation. We also propose that seemingly paradoxical observations in the literature around reduced blood velocity in response to arteriolar constrictions might be caused by a propagation of constrictions to upstream penetrating arterioles. We provide support for pericytes acting as signalling conduits for upstream smooth muscle activation, and erythrocyte deformation as a complementary regulatory mechanism. Finally, we caution against the use of blood velocity as a proxy measurement for flow. Our combined imaging-modelling platform complements conventional experimentation allowing cerebrovascular physiology to be probed in unprecedented detail.

The mammalian brain has evolved complex neurovascular coupling mechanisms to regulate the flow of blood to tissue in response to neuronal activity. However, the biophysical processes underpinning cerebral blood flow regulation are intricate and incompletely understood. For example, it is known that mural cells, which line the walls of cortical blood vessels, act as an intermediary between neural activity and blood flow, but the precise mechanisms that define this control are unclear.

Mural cells are composed of both arteriolar and venular smooth muscle, and capillary pericytes. It is generally accepted that arteriolar smooth muscle cells (SMCs) are contractile cells which have a role in regulating CBF. It has been suggested that due to the perivascular location and morphology of pericytes, these cells may also be contractile[1]. Similarly, studies suggest that neurotransmitter-mediated signalling plays a key role in regulating CBF by contributing to the vascular tone of capillaries as well as arterioles[2–4]. However, their involvement in the CBF regulation remains controversial[5].

In vivo experiments that aim to probe these mechanisms present a range of technological challenges, and typically provide limited spatial and temporal information. Increasingly, mathematical modelling is being used to provide a precisely controlled, alternative tool for investigating biophysical phenomena[6–12], particularly when accompanied by corroborating *in vivo* data.

In this study, we sought to develop a novel mathematical modelling platform that used structural data from *in vivo* imaging of the mouse cortex upon which to simulate the complex physiology and fluid dynamics of the cerebral vasculature. The extraction of cerebral vascular network structure enabled the parametrisation of two comprehensive, coupled mathematical models for blood flow and oxygen transport, which facilitated physiologically realistic *in silico* experiments to be performed. These allowed us to examine the complex interactions between coupled physiological phenomena, occurring in spatially isolated regions within the cortical vasculature.

Our novel modelling approach inputs data on the location of vessels surrounded by SMCs, which were derived from *in vivo* two-photon imaging of a genetic reporter of alpha-smooth muscle actin (α-SMA). SMCs

[1]Mechanical Engineering, University College London, London, UK. [2]Centre for Advanced Biomedical Engineering, University College London, London, UK. Correspondence and requests for materials should be addressed to R.J.S. (email: rebecca.shipley@ucl.ac.uk)

are included in the four morphological classes of mural cells that are thought to have an influence on CBF regulation[13]. SMCs surround the entire circumference of pial and penetrating arterioles (with diameters in the range 15 to 40 μm), precapillary arterioles (diameters ranging from 3 to 15 μm) and postcapillary venules, whilst capillary pericytes are found on microvessels with diameters of 3 to 9 μm. Conversely, capillary pericytes within the cortex do not express α-SMA, which is thought to be a necessary prerequisite for contraction. It remains unclear which of these vessel types has the greatest impact on CBF regulation, therefore this formed the basis for our investigations.

Of particular interest given our fluid mechanics approach, were reports of decreases in blood velocity following vasoconstriction[13,14] or increases in velocity following vasodilation[2,15,16]. According to Poiseuille's law, which relates blood pressure and the volumetric flow rate to vessel diameter, a local decrease in vessel diameter should induce a localised velocity increase, assuming the volumetric flow rate is approximately maintained, rather than the decreases observed *in vivo*. Such a response is expected even when allowing for variation in localised blood flow. These paradoxical observations suggested to us that the observed vasomodulations could be related to changes occurring on the scale of the network, and which could be meaningfully investigated with a large-scale numerical modelling approach.

Alongside vessel diameter changes, we were also interested in probing alternative mechanisms that have been proposed for regulating CBF. For example, Wei *et al.*[15] suggest that erythrocytes act as O_2 sensors and can alter their shape in order to modify blood flow and vascular O_2. Questions remain regarding how erythrocytes can actively deform, if erythrocyte modulation couples with arteriolar hyperaemia and if cognitive decline in various diseases is a result of impaired PO_2-mediated capillary hyperaemia. However, combining each of these mechanisms in a comprehensive mathematical model allowed us to study them in much greater detail than could be achieved in a conventional experimental setting.

Our mathematical modelling provided additional, detailed insights into volumetric flow, haematocrit and PO_2 changes within blood vessels and cortical tissue. These have enabled us to form a clearer understanding of the mechanisms underpinning CBF regulation, which we present here, and which have implications for the interpretation of future *in vivo* experiments.

Results

Simulation of blood flow and oxygen delivery in the mouse cortex. Our study used *in vivo* imaging data from the mouse cortex, acquired with a two-photon microscope (Praire Technologies). We acquired image data from adult male SMA-mCherry transgenic mice[17], which enabled cortical α-SMA on the surface of arterioles to be detected via the fluorescence of mCherry (800 nm excitation). Cascade Blue Dextran (800 nm excitation) was also injected intravenously, to allow the simultaneous imaging of blood vessel lumen. Image volumes had dimensions of $420 \times 420 \times 400$ μm^3 and resolution of $2.4 \times 2.4 \times 4$ μm^3 (see Fig. 1a,b). During post-processing, we segmented blood vessel lumen and smooth muscle regions using in-house software, and converted the data into a graph format consisting of nodes and connecting segments. These data provided the geometrical inputs of a single cortical network for our mathematical models. Each vessel had an associated diameter and a flag denoting the presence or absence of smooth muscle coverage (see Fig. 1c).

Our mathematical model was written in C++[18] in which Poiseuille flow was modelled through individual vessel segments, and was coupled to a Green's function model for intravascular and tissue oxygen transport[19]. Our model enabled a complex, quantitative assessment of blood flow within large cortical networks, and included the non-Newtonian effects of blood and haematocrit heterogeneity through application of empirical laws[20]. Boundary conditions for the model were assigned according to previously published computational data[6,7]. Diameter-dependent pressure conditions were assigned to all pial boundaries, with inlet haematocrit set to 0.45, allowing flow solutions to be calculated that minimised the deviation from target pressures and vessel wall shear stresses[21]. Similarly, boundary PO_2 was assigned based on experimental data[12,22], thereby enabling physiologically-accurate solutions.

Our first simulation run provided a "baseline" flow and O_2 solution, using vascular network architecture derived from imaging data (see Fig. 1d,e,f). This returned a vascular perfusion of 147.1 ml/min/100 g, which is in good agreement with previous studies[23,24], whilst mean tissue PO_2 (partial oxygen pressure) was calculated as 29.3 mmHg (with a computed oxygen extraction fraction of 0.47 - see Supplementary Video). Flow velocities, mean PO_2 and SO_2 (oxygen saturation) were also in the range of previous experimental measurements[15,22] and computational studies[10] (see Table 1 and Supplementary Fig. S1). This agreement between our simulation results and literature values gave us confidence that our model could provide physiologically-realistic solutions.

Optogenetically-induced constrictions in arteriolar smooth muscle propagate to upstream arterioles and induce blood velocity decreases. Hill *et al.*[13] performed single-cell mural constrictions using confocal laser line-scanning to activate ChR$_2$ (channelrhodopsin 2). Single-cell constrictions, in which individual mural cells are activated, induced a reduction in vessel diameter. In order to prevent proximal vessel constrictions via the confocal laser, targeted two-photon stimulation of ChR$_2$ within small areas of interest along single vessels, was also used to measure the resultant blood velocity modulations at the site of constriction. As a second validation of our model, we performed an *in silico* experiment to replicate this type of intervention.

Following Hill *et al.*[13], constrictions were simulated in three vessel types: 1) penetrating arterioles (smooth muscle coverage and a diameter > 10 μm), 2) precapillary arterioles (smooth muscle coverage and diameter < 10 μm, at the arteriolar/capillary interface) and 3) capillaries (no smooth muscle coverage, and first branching order from the arteriolar/capillary interface). Consistent with those measured by Hillet *et al.*[13], we reduced vessel diameter by -19.41, -11.79 or -0.1% (representing peak diameter changes for vessel types 1–3, respectively), in a series of 25 simulations each containing a localised, single-cell constriction (10 μm in length).

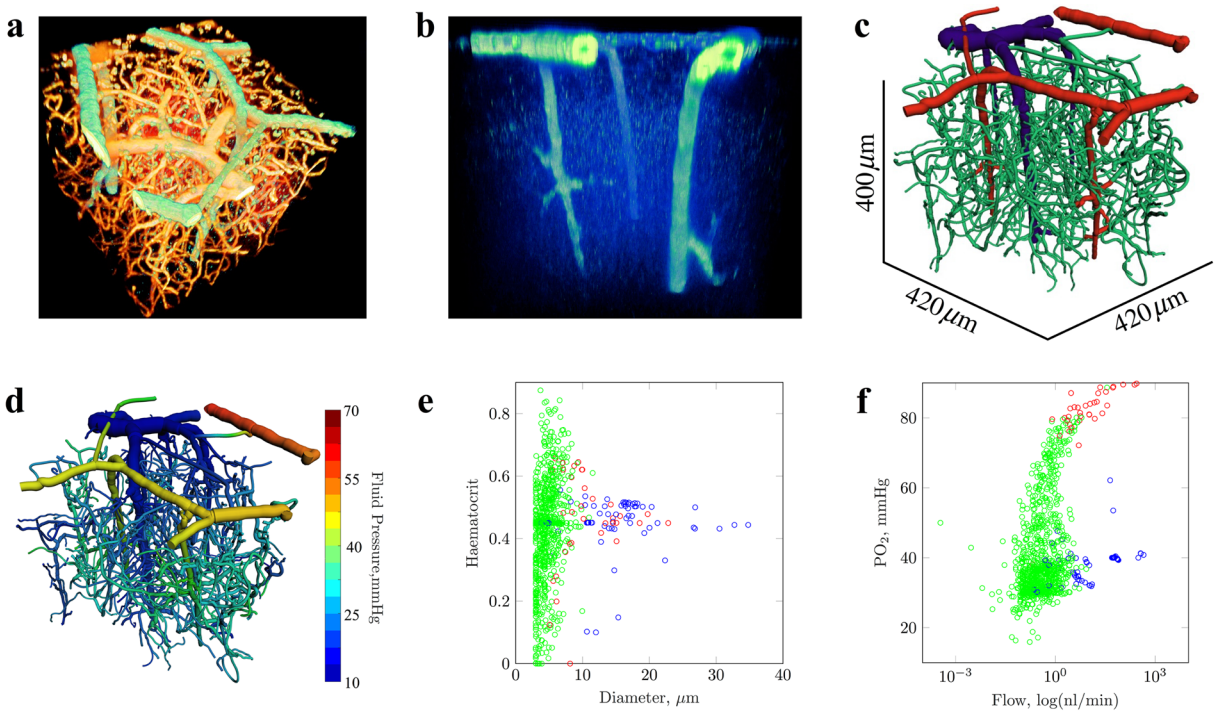

Figure 1. Mathematical modelling of blood flow in the cortical microvasculature, using 3D confocal imaging data from transgenic mice. (**a**) A view of the cortical vascular network showing smooth muscle actin-covered vessels (SMA, green), from transgenic expression of m-Cherry, and blood vessel lumen (orange), from exogeneous administration of fluorescent dextran. (**b**) An enhanced view showing the location of SMA-expressing vessels. (**c**) The vascular network, following image segmentation, with vessels colour-coded based on classification (red: SMA-expressing arterioles; blue: veins; green: capillaries). (**d**) Simulated cortical blood pressures within the cortical network. (**e**) A scatter plot of vessel diameter against simulated, blood vessel haematocrit from our baseline simulation. (**f**) A scatter plot of volumetric blood flow (nL/min) against intravascular PO_2 (mmHg). Data points in (**e**) and (**f**) are colour-coded according to vessel classification, as per (**c**).

	Vessel Class			
Parameter	**Arteriole**	**Capillary**	**Venule**	**Unit**
Pressure	50.6 ± 8.7	28.8 ± 6.1	19.3 ± 2.1	mmHg
Flow	55.5 ± 84.7	0.67 ± 2.02	73.6 ± 124.4	nl/min
Velocity	4.1 ± 3.9	0.56 ± 0.94	3.1 ± 3.7	mm/s
PO_2	83.5 ± 6.1	40.7 ± 13.1	38.0 ± 4.6	mmHg
SO_2	85.4 ± 3.4	46.9 ± 16.0	45.6 ± 6.6	%

Table 1. Blood flow and oxygenation summary statistics, for the baseline simulation (data are mean $\pm$ standard deviation).

For single-cell constriction of penetrating and precapillary arterioles, we found a large increase in blood velocity of 53.0 ± 1.6 and 27.5 ± 2.8%, respectively, within the constricted vessel. This increase in velocity at the point of constriction is to be expected, according to fluid dynamical models, and is analogous to constricting a hose pipe, in which fluid velocity increases to conserve mass. However, this conflicts with the observations by Hill *et al.*[13], and others[14], who observed a velocity decrease following vessel constriction. This presents a paradox that we sought to resolve.

During functional hyperaemia, vessel dilations can be propagated upstream from the initial site of activation[25]. We hypothesised that optogenetic SMC activation could result in a cascade of vasoconstriction in its local vicinity. We therefore explored three scenarios in addition to single-cell constriction (scenario 1 - see Fig. 2); constriction of a single-cell initiating a cascade of constriction: 2) extending to the nearest vessel branching points (single vessel constriction); 3) upstream to the nearest penetrating arteriole and then propagating in both directions perpendicular to the cortical surface (bi-directional cascade); and 4) upstream to the nearest penetrating arteriole and then propagating upstream towards the cortical surface (uni-directional cascade). For consistency, these cases were also investigated for capillary constrictions.

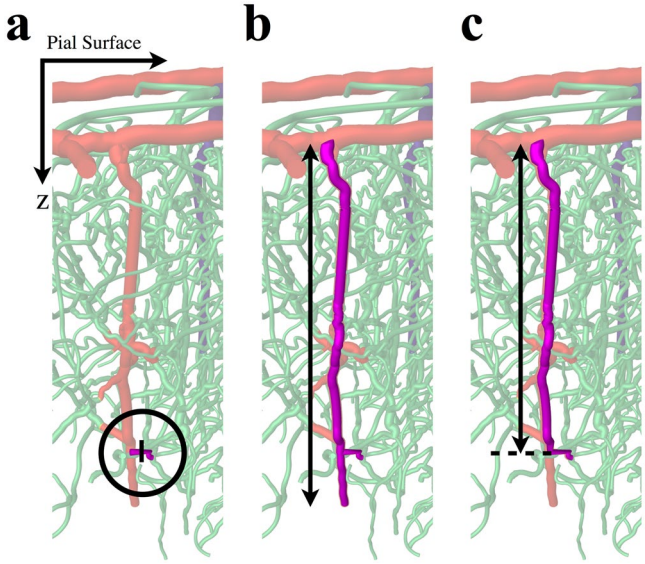

Figure 2. Sites of simulated blood vessel constrictions in SMA-expressing vessels (purple). (**a**) The location of single branching-order precapillary arteriole constriction (circled); the black line indicates the site of a single-cell constriction. (**b**) Constriction of a precapillary arteriole, with bi-directional constriction cascade to the entire adjoining penetrating arteriole. (**c**) Constriction of a precapillary arteriole and uni-directional propagation to upstream sections of the penetrating arteriole. The dashed line indicates the point at which the penetrating arteriole bifurcates to the precapillary arteriole.

We found that, for bi-directional propagation, mean blood velocity increased in penetrating arterioles (see Fig. 3a). In the case of uni-directional propagation, the constricted vessel exhibited a velocity increase of $25.9 \pm 12.4\%$, but unconstricted, downstream vessels exhibited a velocity decrease of $11.7 \pm 8.0\%$, which is consistent with *in vivo* experiments[13,14].

We observed blood velocity changes of $17.6 \pm 6.6\%$ and $-5.2 \pm 14.4\%$ in constricted precapillary arterioles for scenarios 1 (single vessel constriction) and 2 (bi-directional cascade), respectively (see Fig. 3b). Similarly, uni-directional propagation caused blood velocity in constricted precapillary arterioles to decrease by $22.2 \pm 8.0\%$, a magnitude of change that is more consistent with that found *in vivo*[13], and so we discounted scenarios 1 and 2 (see Supplementary Tables S4–S7 for additional statistics on haemodynamic response). This outcome suggests that optogenetically-induced constrictions of SMA-covered precapillary arterioles propagates upstream along its local penetrating arteriole. These physiologically-plausible results suggest a resolution to the paradoxical *in vivo* observations of a decrease in blood velocity following blood vessel constriction. It is only by significantly increasing the resistance to blood flow by propagating diameter reductions to a much larger section of upstream vessels, that we observe a velocity decrease in response to vessel constriction. It is also plausible that this mechanism can explain similarly paradoxical increases in blood velocity observed following induced vessel dilations of cerebral arterioles.

Optogenetically-induced constriction of capillary pericytes does not induce constriction propagation. Our simulations found that constriction of capillary pericytes produced a blood velocity increase of $1.3 \pm 3.4\%$ within the constricted vessel. This is consistent with *in vivo* observations that capillary diameter changes contribute minimally to changes in blood velocity[13]. For consistency, uni- and bi-directional constriction cascades were also investigated for capillary constrictions.

When constrictions were initiated across single capillary branches, we found blood velocity decreased by $1.0 \pm 8.3\%$. As with single-cell constriction, minimal changes in blood velocity occurred (see Fig. 3c). As pericytes are known to span along entire vessels[13,26], whole vessel constriction is arguably a more physiologically representative intervention than the 10 μm 'single-cell' activation. Inducing bi- and uni-directional constriction cascade, passing from perictyes to SMA-covered vessels, produced velocity decreases far in excess of the variations observed *in vivo*[13] (-9.6 ± 21.1 and $-18.6 \pm 25.3\%$, respectively - see Fig. 3c). As such, our results suggest that optogenetically-induced constriction of capillaries, via capillaries, does not induce a cascade of constriction along local SMA-covered arterioles.

The relationship between vasoconstriction and haemodynamic changes is non-trivial. In our simulations, following single vessel constriction, blood flow in penetrating and precapillary arterioles decreased by 0.6 ± 1.0 and $0.6 \pm 2.2\%$, which further decreased to $-39.5 \pm 13.2\%$ when uni-directional constriction cascade was introduced (see Fig. 3d,e). However, blood velocity showed changes in the opposite direction, with an increase of 53.0 ± 1.6 and $17.6 \pm 6.6\%$ for penetrating and precapillary arterioles, and a change of 35.9 ± 12.4 (-11.7 ± 8.0 downstream of constriction) and $22.2 \pm 16.9\%$ when uni-directional propagation was introduced. Mathematically, these opposite changes in blood flow and blood velocity observed within penetrating arterioles are a distinct possibility (see Supplementary Note). Therefore, we advise caution against the use of blood velocity as a proxy measurement for flow.

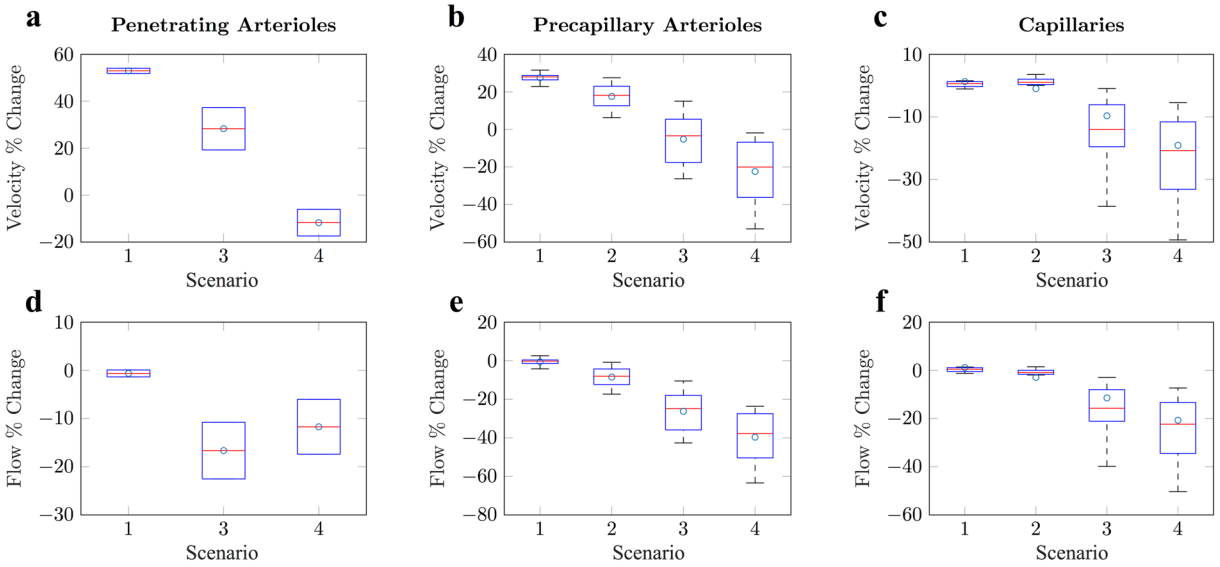

Figure 3. Box plots showing simulated blood velocity and flow changes in response to vasoconstriction. The top row of graphs shows blood velocity changes as a percentage of the baseline solution, and the bottom row shows blood flow changes. From left to right, plots show the responses to constrictions in penetrating arterioles (left), precapillary arterioles (middle) and capillaries (right). Results are presented for each constriction scenario (1) single-cell constriction, (2) constriction of the entire vessel, (3) bi-directional and (4) uni-directional constriction of the local penetrating arteriole. Note, cases (2) and (3) are equivalent for penetrating arterioles and the mean values for each are indicated with circles. Case 4 for penetrating arterioles provides the velocity change for the neighbouring downstream vessel from the site of constriction. Mean values are indicated in blue. See Supplementary Fig. S2 for outliers.

Within capillaries, this non-trivial relationship between blood velocity and flow becomes more complex due to the increased influence of flow resistance instigated by the restricted passage of erythrocytes (Supplementary Fig. S3). Our simulations of constrictions in SMA-covered vessels, initiated by pericyte constriction, showed that reductions in blood flow and velocity were mediated by decreases in blood pressure and blood viscosity, compared to pressure alone in SMA-covered vessels (see Tables S6 and S7, respectively). Since our results suggest that optogenetic-induced constriction of pericytes does not induce a cascade of constriction along vessels, these data suggest that dynamically altering blood viscosity within capillaries may provide the most optimal means to regulate capillary hyperaemia.

Nano-scale, single-capillary pericyte constrictions have a variable and spatially heterogeneous effect on tissue PO_2. Having investigated the effect of vasoconstriction on blood flow and velocity, we turned our attention to the impact of these changes on intravascular and tissue PO_2.

The recent study by Kisler *et al.*[16] demonstrated that pericyte loss-of-function weakens capillary ability to modify CBF following neuronal stimuli, leading to neurovascular uncoupling and reduced oxygen supply. It was suggested that the inhibited ability of a capillary to dilate following pericyte dysfunction relates to tissue PO_2 regulation. However, Hill *et al.*[13] observed minimal vasomotion in pericyte-covered capillaries (a $0.08 \pm 0.18\%$ change in diameter) following optogenetic-activation and, in addition, our results show that at peak constriction, only small changes were exhibited in both blood velocity and flow (unless constriction cascade is introduced). Nonetheless, it is unclear whether these small changes in flow are sufficient to impact cortical oxygenation.

Using our flow constriction solutions, we therefore simulated changes in O_2 transport within the cortical network. We observed changes in capillary PO_2 of -0.6 ± 0.08, -7.8 ± 5.9 and $-9.1 \pm 6.7\%$ for constrictions in penetrating arterioles, precapillary arterioles and capillaries, respectively (which included constriction cascade in SMA-covered vessels - see Fig. 4a,b,c). Tissue PO_2 changed by -13.0 ± 2.4, $-2.7 \pm 0.8\%$ and $0.45 \pm 0.31\%$, respectively (see Fig. 5a,b,c).

This suggests that, even with minimal flow changes, significant reductions in PO_2 were found following nano-scale capillary vasoconstriction, and were similar in size to those exhibited following constrictions in precapillary arterioles. This effect is possible due to the combined effect of small flow reductions alongside vessel haematocrit reductions (-2.9 ± 8.2 and $-2.36 \pm 6.58\%$, respectively), the latter of which plays a much larger role in capillaries than in larger vessels and, in the case of micron-scale dilations, has been hypothesised to be an efficient mechanism that can locally alter the distributions of RBCs in microvascular networks[27].

Nano-scale constriction of capillaries produced a highly variable PO_2 response, with a heterogeneous distribution of both increases and decreases in PO_2 in the vicinity of a constriction. For example, in a $60 \times 60 \times 60$ mm^3 tissue volume centred on the constricted capillary, tissue PO_2 increased by $2.9 \pm 6.6\%$ (rather than an expected decrease; see Fig. 4d), due to the redistribution of haematocrit to neighbouring capillaries.

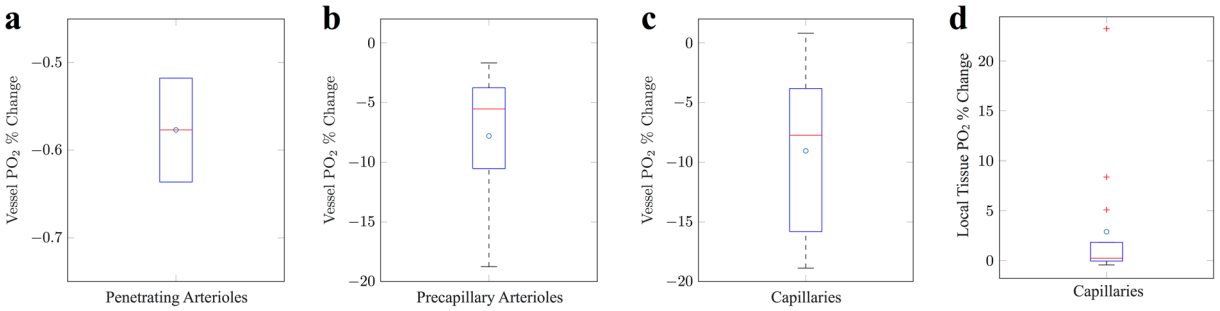

Figure 4. Simulated single vessel constrictions and the subsequent change in vessel and tissue PO_2. Box plots indicated the percentage change in vessel PO_2 in constricted (**a**) penetrating arterioles, (**b**) precapillary arterioles and (**c**) capillaries, when compared to baseline PO_2 in said vessel. Noting, for (**a**,**b**) constriction cascade is induce by constriction of SMA-covered vessels. (**d**) The percentage change in local tissue PO_2 as a consequence of constrictions in (**c**). Mean values are indicated in blue and outliers (data larger than $q_3 + 3(q_3 - q_1)/2$ or smaller than $q_1 - 3(q_3 - q_1)/2$, where q_1 and q_3 are the 25^{th} and 75^{th} percentiles, respectively) by red crosses.

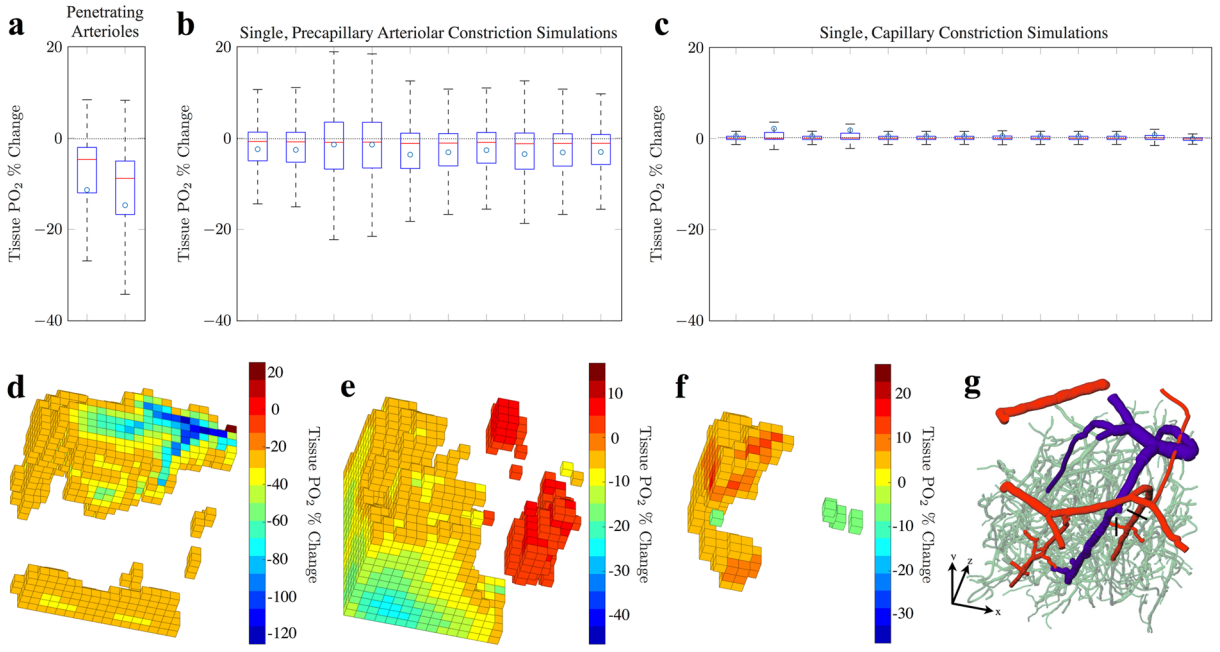

Figure 5. Simulated single vessel constrictions (a total of 25, with constriction cascade induced by constriction of SMA-covered vessels) and the subsequent changes in global tissue PO_2. Box plots indicated the percentage change in tissue PO_2, when compared to baseline tissue PO_2, as a consequence of singular constrictions of (**a**) penetrating arterioles, (**b**) precapillary arterioles and (**c**) capillaries. (**d**,**e**,**f**) 3-dimensional visualisations of spatial changes in tissue PO_2 as a result of constrictions in (**d**) a penetrating arteriole, (**e**) a precapillary arteriole and (**f**) a capillary. (**g**) 3-dimensional visualisation of the cortical network, in which black lines indicate the initial site of constriction for (**d**) and (**e**), and where the capillary constriction in (**f**) occurred downstream of (**e**). Note, absolute percentage changes $< 20\%$ for (**d**) and absolute values $< 5\%$ for (**e**) and (**f**) are not shown, for clarity.

In addition, we found a strong correlation between changes in blood flow and capillary PO_2, which was not evident between changes in blood velocity and capillary PO_2 (see Supplementary Table S3). This suggests that blood flow is a more significant factor in determining PO_2 than blood velocity. The *in silico* study by Lücker *et al.*[28] also found that haematocrit had a larger influence on tissue PO_2 than RBC velocity in lower order capillaries. In combination, this identifies the limitations in drawing inferences about cortical oxygenation from measurements of blood velocity.

Arteriolar constrictions induces stable intravascular capillary and tissue oxygenation changes. We have shown that nano-scale constriction of capillaries leads to a significant reduction in vessel PO_2, yet causes an unpredictable alteration to tissue PO_2 in the local vicinity, due to haematocrit redistribution. In addition, optogenetic activation of capillary pericytes does not appear to induce constriction cascade to local SMA-covered

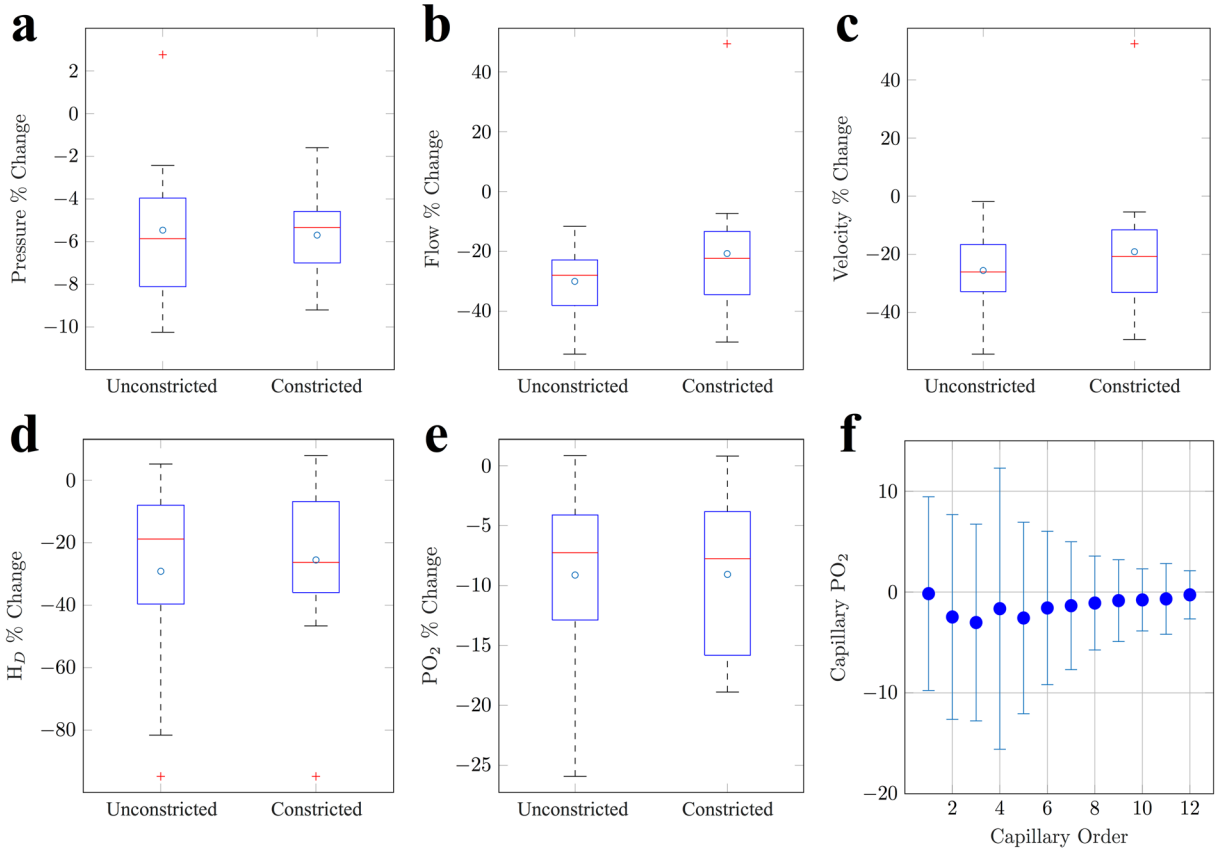

Figure 6. Simulating SMA constriction cascade following pericyte constriction. Percentage changes in: 1) unconstricted and 2) constricted capillaries with uni-directional SMA propagation for (**a**) pressure, (**b**) flow, (**c**) velocity, (**d**) haematocrit (H_D) and (**e**) vessel PO_2. (**f**) A plot of mean change in capillary PO_2 against capillary order, as a result of local SMA constriction. Error bars represent standard deviation and, consequently, the redistribution of O2 through the cortical network.

arterioles. However, due to the complex molecular mechanisms surrounding pericyte activation[2,3], under normal physiological conditions, this effect could occur via other signalling pathways, which may then induce more stable and predictable regulation of local tissue PO_2 surrounding capillaries. Based on this hypothesis, we investigated the effects of simultaneous constriction of a capillaries with uni-directional constriction cascade to local SMA-covered vessels. The results of these simulations were then compared with those in which capillaries remain unconstricted, but constrictions were propagated to SMA-covered vessels.

Our results show that local constriction of SMA-covered vessels had a similar, if not greater, impact on capillary haemodynamics than when coupled to capillary constriction (see Fig. 6a,b,c,d,e). SMA constriction caused intravascular capillary PO_2 at unconstricted sites to reduce by $9.1 \pm 7.3\%$, led by a greater reduction in capillary flow and haematocrit (30.0 ± 11.5 and $29.2 \pm 30.1\%$, respectively). In comparison, constriction cascade to SMA-covered vessels, coupled with capillary constriction, reduced PO_2, flow and haematocrit by a similar or diminished amount: 9.1 ± 6.7, 20.7 ± 24.9 and $25.5 \pm 26.8\%$, respectively.

We next analysed the impact of SMA constriction cascade on each capillary branching order, which showed that local SMA cascade in the absence of pericyte-led constriction can effectively alter downstream capillary intravascular PO_2 (see Fig. 6e,f) in addition to reducing tissue PO_2. These results suggest that SMA constriction cascade, led by precapillary arterioles, does not necessarily need to be coupled to pericyte capillary constriction in order to actively regulate the passage of intravascular and interstitial O_2. Thus, our simulations suggest that SMA-covered vessels have the capacity, in isolation, to regulate blood flow and oxygenation in a targeted and predictable manner throughout the cortex.

Functional erythrocyte deformability has the capacity to drive capillary hyperaemia. Precapillary arterioles and capillaries adjacent to penetrating arterioles offer the greatest contribution to hydraulic resistance[10], supporting the accepted view that changes in blood vessel diameter can effectively regulate blood flow. We have demonstrated that constriction via smooth muscle dynamically alters blood flow, velocity, fluid pressure and PO2. However, a hypothetical mechanism proposed by Wei *et al.*[15], suggests that erythrocytes can deform in response to low vessel PO2, causing a reduction in blood viscosity[15] (but without initially altering blood haematocrit) and therefore a decline in flow resistance.

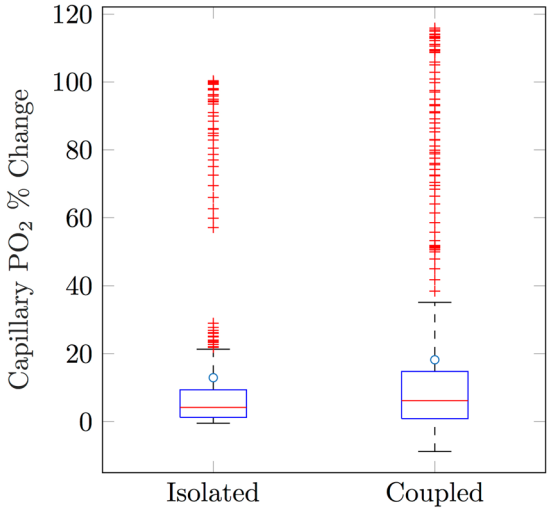

Figure 7. Capillary PO_2 changes initiated by erythrocyte deformation. Box plots show the percentage change in PO_2 for capillaries initially below 25 mmHg, for erythrocyte deformation occuring in isolation, and when coupled to arteriolar (SMA) dilation.

This formed the basis for our next set of simulations, in which our baseline cortical flow solution identified capillary vessels that exhibited PO_2 lower than 25 mmHg (1.7% of all capillary segments), these became sites for spontaneous erythrocyte deformation (instantaneous elongation). We reduced blood viscosity in these vessels by 20% to mimic the effects of erythrocyte deformation.

We found that spontaneous erythrocyte deformations increased blood velocity, on average, by $9.8 \pm 6.2\%$ (with equivalent changes in flow). This is consistent with the peak velocity changes measured empirically by Wei *et al.*[15], and was accompanied by an average vessel PO_2 increase of $12.9 \pm 24.3\%$. This provides support for the hypothesis that spontaneous erythrocyte deformation is a plausible mechanism for increasing vessel PO_2. Given that our results suggest that SMA-covered arterioles can dynamically alter capillary PO_2, we performed a further simulation to investigate the combined effect of arteriolar diameter changes, alongside erythrocyte deformation. We induced a diameter dilation of 4.5%[15] to all SMA-exhibiting vessels (excluding pial vessels) alongside erythrocyte deformation in capillaries with low-oxygen tolerance (as defined above). On average, velocity and flow increased in these capillaries by $10.7 \pm 5.7\%$, and PO_2 increased by $18.2 \pm 31.3\%$. This result shows that global arteriolar dilation coupled to erythrocyte deformation amplified the PO_2 change in these capillaries on average by 41.1%, compared to isolated deformation.

We also found that a large subset (97.4%) of capillaries exhibited a marked increase in blood flow and PO_2 in response to erythrocyte deformation, both when modelled in isolation, and when erythrocyte deformation was coupled to arteriolar dilation (see Fig. 7). This could limit the efficacy of erythrocytes for providing targeted, isolated changes in tissue oxygenation that are not compromised by neighbouring regions. However, whether such effects have a significant impact on neurovascular coupling would require further investigation. Likewise, whilst our simulations strongly implicate SMA-covered vessels as the main modulatory apparatus for cortical oxygenation, they are unable to determine the mechanism that triggers such a response from the capillary level. Rather, our simulations indicate that both erythrocyte deformation and pericyte signalling are both plausible mechanisms, and worthy of experimental investigation.

Discussion

The regulation of cortical blood flow has been studied extensively, yet details of the mechanisms underpinning its precise control remain elusive. This is due in part to the multiplicity of potential influences, which are interdependent and challenging to isolate empirically. We therefore sought to develop an original paradigm, composed of both *in vivo* imaging and mathematical modelling, to explore cortical microcirculatory blood flow and oxygen transport regulation mechanisms in a block of mouse cortex, imaged using a two-photon microscope *in vivo*.

The mathematical models which constitute our *in silico* platform have been thoroughly tested and validated in previous computational studies in order to accurately simulate blood flow[6,7,9,11,12,21,29,30] and oxygenation[19,30,31] in physiological microvascular networks. In addition, our platform has been parametrised and the results compared against a wealth of experimental data[12–15,22–24,32–34] in order to validate its simulations.

A key advantage of our modelling approach is its ability to provide complete network flow, haematocrit and oxygen distributions, simultaneously, which would be impossible to obtain in a conventional experimental context. This also allowed us to perform novel, controlled *in silico* experiments on a real-world cortical network structure. By recreating experimental designs from the literature, *in silico*, such as by Hill *et al.*[13] and Wei *et al.*[15], we have demonstrated the ability of our paradigm to reproduce physiologically realistic solutions and provided further physiological insights. In contrast to previous studies, our study combined *in vivo* genetic cell labelling and mathematical modelling to probe cortical microvascular structure and function, which are otherwise unavailable in isolation.

Hill *et al.*[13] provided an excellent start point, as this study provided detailed *in vivo* measurements of blood velocity in multiple vessel types, following vessel constriction. They demonstrated that activation of SMC-covered arterioles in mouse cortex caused a significant decrease in diameter ($-19.41 \pm 1.9\%$) and blood velocity ($-44.62 \pm 11.8\%$), whereas blood vessels covered by pericytes showed no significant change in either diameter or velocity ($-0.08 \pm 0.18\%$ and $-2.22 \pm 3.16\%$, respectively). This reported decrease in blood velocity in response to constriction of SMA-covered arterioles (using optogenetic stimulation) presented a paradox, given that Poiseille's law predicts that, by decreasing vessel diameter, blood velocity should increase assuming the volumetric flow rate is approximately maintained (in contrast, with an increase in vessel diameter, blood velocity should decrease). Our simulations explain this paradox if this localised activation induces a cascade of upstream constrictions, from precapillary arterioles to descending penetrating arterioles. The increased flow resistance induces a velocity decrease of similar magnitude to that measured experimentally in Hill *et al.*[13]. This propagation mechanism has previously been demonstrated by Dietrich *et al.*[35] and in subsequent studies[25], in the instance of arteriolar dilation, and our simulations provide strong support for this effect in the case of arteriolar constriction.

Invoking constriction propagation enabled us to suggest a resolution to the paradoxical observations of blood velocity decrease in response to vasoconstriction, but also demonstrated a non-trivial relationship between changes in blood velocity (directional speed) and blood flow (volume transfer per unit time) following vasoconstriction. Conversely, flow was strongly correlated with capillary oxygenation. Poiseuille's law forms the basis of our model and is often invoked in the literature to link changes in blood velocity to blood flow through a single vessel. However, our results show that this may not always be the case as it does not incorporate the network flow response, nor the redistribution of haematocrit. Our results suggest that it is possible for a vessel to exhibit an increase in blood velocity, post-constriction, whilst observing a reduction in flow. Therefore, caution is needed when inferring flow changes from measured blood velocity changes; blood velocity is a poor proxy for flow or oxygenation.

Constriction propagation was not necessary to explain Hill *et al.*'s[13] velocity changes in response to capillary pericyte activation. When we simulated constriction cascade from capillaries, velocity decreases were far in excess of *in vivo* measurements. However, we cannot infer whether this is a nuance of optogenetic activation, or if constriction cascade cannot be propagated from capillary pericytes. Likewise, isolated capillary constrictions induced minimal blood flow changes, compared with arteriolar constrictions.

It is accepted that smooth muscle cells control arteriolar hyperaemia, however the mechanisms controlling capillary hyperaemia are debated[2,13,16] and the role of pericytes remains controversial. The capacity of pericytes to modulate cerebral blood flow has been measured *in vivo* through vasoconstriction[13] and vasodilation[2,16], with data (inferred from velocity measurements) suggesting that capillaries contribute minimally to variations in CBF[13]. Conversely, pericyte dysfunction has also been linked to neurovascular uncoupling[17]. Our simulations showed that nano-scale constrictions are able to significantly alter capillary and tissue PO_2, although the resultant changes were spatially heterogeneous, with constriction-induced velocity decreases accompanied by both increases and decreases in nearby capillaries. This variation across the network was due to the redistribution of blood flow and haematocrit to neighbouring vessels. Interestingly, flow and oxygenation changes caused by constriction cascade from capillaries to arterioles were similar if not smaller than when propagation of arterioles emanated solely from local precapillary arterioles.

Our results therefore suggest that arterioles have the capacity to regulate capillary hyperaemia without the need for pericyte-led capillary constriction. Hall *et al.*[2] suggested that, due to their proximity to neurons, neuronal signalling to pericytes occurs before signalling to smooth muscle. Additionally, Kisler *et al.*[16] demonstrated that pericyte-deficient mice had a diminished oxygen supply to the cortex. As such, we hypothesise the pericytes may purely act as signalling conduits to upstream arteriolar smooth muscle, allowing for a localised vasomotion response by arterioles. Any pericyte-led neurovascular uncoupling may inhibit signalling to local arterioles and thereby reduce the ability to regulate cortical O_2. In summary, our results suggest that arterioles have the capacity to dynamically modulate both arteriolar and capillary hyperaemia in a coordinated and stable fashion.

However, other (potentially complementary) regulation mechanisms have also been proposed in the literature. We investigated the recent hypothesis that erythrocytes act as O_2 sensors which regulate their own deformability in order to increase flow velocity in response to low PO_2[15]. We reduced blood viscosity in vessels below a PO_2 threshold in order to mimic the drop in flow resistance observed experimentally[15]. The subsequent velocity changes as a result of erythrocyte deformation correlated well with peak velocity changes seen *in vivo*[15] and flow increases resulted in significant PO_2 increases within selected capillaries with further increases exhibited when coupled to global arteriolar dilation. This provides support for erythrocyte deformation as a plausible mechanism for regulating vascular PO_2 and cerebral blood flow. However, this functional response requires further empirical investigation to determine, for example, the scale of erythrocyte deformation and its ability to dynamically alter tissue PO_2 (which can then be more precisely modelled).

Our results provide support towards a range of biological phenomena, however we provide caution to its following limitations. Firstly, simulations were performed on a single cortical microvascular network. The cortex displays spatial heterogeneities in architecture across equivalent samples[36], which may incur a varied response from duplicate simulations. Thus, future work should seek to reproduce our study across multiple cortical networks. Secondly, the choice of boundary conditions has been shown to strongly influence the flow field[7,21]. The method we have applied uses a reduced number of unknown parameters (e.g. target shear stress and pressures for the network) to estimate flows and pressures throughout the network, compared to estimating all boundary values individually. However, sensitivity to these target values is minimal[21]. As a result, our method is more robust to perturbations than alternative methods. Future simulations should be composed of boundary condition assignment validated against *in vivo* blood flow measurements specific to the network being studied. This would provide a rigorous approximation of blood flow through the cortical microvasculature.

The limited size of the network used in this study meant that the effects of vascular steal from adjoining vascular networks could not be studied in detail, and larger networks could provide further insights. It would be of interest to investigate the influence of erythrocyte deformability incorporated to facilitate O_2 regulation under pathophysiological conditions[15]. Likewise, capillaries have been observed to dilate in response to micro-occlusions[37], potentially suggesting a more dynamic response via the vascular network than we were able to simulate here. Each of these effects can be further explored in future studies, placing our modelling platform in an ideal position to perform detailed hypothesis-testing.

We have established a novel platform which combines *in vivo* cortical microvascular data with computational models to gain insights into cerebral blood flow regulation and oxygen delivery. This platform has enabled a thorough understanding of mural cell contribution to cortical haemodynamics, and the formulation of hypotheses that had not arisen from the *in vivo* work in isolation. For example, we have proposed that optogenetic stimulation of SMA-covered arterioles induces a cascade of upstream constrictions and that such activation of pericytes does induce an equal response. Also nano-scale constrictions of pericyte covered capillaries can significantly alter capillary PO_2, although these changes are spatially heterogenous. In comparison, arterioles have the capacity to hyperaemia without the need for pericyte-led capillary constriction, suggesting pericytes may purely act as signalling conduits to upstream arteriolar smooth muscle. Moving forwards, we anticipate that the findings from this work will give rise to new experimental and mathematical modelling research to further our understanding of neurovascular coupling in both health and disease.

Methods

Animal Experiments. All animal procedures were approved by the Institutional Animal Care and Use Committee (IACUC) at Yale University, with all methods performed in accordance with the relevant guidelines and regulations. We acquired our images from adult male SMA-mCherry transgenic mice[17] aged 120 days housed in a 12:12 light:dark cycle animal vivarium with food and water provided ad libitum. We performed acute craniotomies to acquire *in vivo* two-photon fluorescence based microvascular three-dimensional reconstructions. Briefly animals were anaesthetised via intraperitoneal injections of ketamine (100 mg/kg) and xylazine (10 mg/kg) anaesthetic and a 3 mm craniotomy was performed over the somatosensory cortex. The underlying dura was removed and a #0 cover glass was placed over the craniotomy. To visualise the microvasculature, Cascade Blue Dextran (10,000 mw, ThermoFisher Cat# D1976) was injected intravenously prior to imaging. Images were acquired on a two-photon microscope (Prairie Technologies) equipped with a mode-locked MaiTai laser (Spectra Physics) with a 20 × water immersion objection (Zeiss 1.0 NA). Excitation of Cascade Blue Dextran and mCherry in SMA-mCherry mice was achieved using 800 nm two-photon excitation. A full outline of the methods used is outlined in Hill *et al.*[13].

Network Segmentation. Image segmentation was undertaken through thresholding, where we set threshold levels by visual inspection to isolate high intensity fluorophore signals from background noise, for both dextran and mCherry (SMA) signals. For dextran signals, discontinuities within the network, mostly due to imaging artifacts and absent dextran within vessel lumen, were corrected manually in Amira (FEI, Oregon, USA). Thresholded data were thinned using a skeletonisation algorithm[38] and converted to a segment and node format in Amira. We determined SMA coverage, for each vessel, by the distance of each blood vessel centerline to mCherry-positive voxels using in-house software written in IDL (Harris Geospatial Solutions, Boulder, Colorado, USA). If positive signal was detected within 1.5 vessel radii, over at least 90% of a vessel's length, then we categorised that vessel as positive for SMA coverage. This process enabled reconstruction of the cortical microvasculature with vessel classification based on SMA expression, as shown in Fig. 1.

A summary of network statistics (for example, vessel diameters, lengths and classifications) is shown in Supplementary Table S1. We segmented the vascular network into a series of interconnected nodes and segments, where each segment was assumed to be a cylindrical tube. The final network consisted of 26,662 segments, connected by 25,678 nodes, of which 388 were boundary nodes. As venules were not classified by SMA expression, non-SMA vessels above a threshold of 8 μm were identified and those forming a connected tree-like structure were categorised as venules.

Mathematical Blood Flow Model. The mathematical model was coded in C++ and is comprised of the discrete network flow model of Pries *et al.*[39] alongside the flow estimation algorithm of Fry *et al.*[21], where the structural properties of the segmented network and hemodynamic parameters are used as inputs. Here we presented the mathematical models followed by a section on boundary condition (BC) and parameter assignment. The discrete-network blood flow model has been thoroughly tested using mesenteric networks[34] in which blood flow measurements were taken in individual vessels[20,21,39,40] with equivalent models applied to cortical networks[6,7,9].

For our cortical microvascular network, no flow or pressure conditions are known at boundaries of the tissue. The method by Fry *et al.*[21] extends the discrete network flow model of Pries & Secomb[20] to networks in which BCs are unknown, based on the concept that the microcirculation is regulated in response to signals relating to flow and shear stresses[41]. The scheme estimates unknown BCs by minimising the squared deviation from specified target network wall shear stresses and pressures values derived from independent information about typical network hemodynamic properties. In essence, the algorithm removes the need to define conditions at all boundary nodes, to one where simulation sensitivity is weighted towards the definition of these two target parameters.

Our segmented microvascular network (see Fig. 1) is represented by a series of vessel segments connected by nodal junctions or, in the case of boundary nodes, one-segment nodes which form a boundary to the microvascular network. We defined a positive flow direction from the start node to end node of each vessel segment. Under

the assumption of Poiseuille flow and conserving flow at blood vessel junctions, the relationship between nodal pressures, p_k and the boundary boundary fluxes Q_{0i} is given by

$$\sum_{k\in N} K_{ik}\, p_k = -Q_{0i}, \quad i \in I \bigcup B, \tag{1}$$

where N is the set of all nodes, I is the set of all interior nodes and B is the set of all boundary nodes with known BCs. For all interior nodes, conservation dictates that $Q_{0i} = 0$, however, if i is a known boundary node, Q_{0i} is the inflow (or outflow if negative). Note, at least one pressure BC needs to be assigned for a unique solution. The matrix K_{ik} represents network conductivity

$$K_{ik} = \sum_{j\in S} L_{ij} M_{jk}, \tag{2}$$

where S is the set of all segments,

$$L_{ij} = \begin{cases} -1, & \text{if } i \text{ is the start node of segment } j, \\ +1, & \text{if } i \text{ is the end node of segment } j, \\ 0, & \text{otherwise,} \end{cases} \tag{3}$$

and

$$M_{jk} = \begin{cases} +\pi d_j^4/(128\mu_j l_j), & \text{if } k \text{ is the start node of segment } j, \\ -\pi d_j^4/(128\mu_j l_j), & \text{if } k \text{ is the end node of segment } j, \\ 0, & \text{otherwise,} \end{cases} \tag{4}$$

is the matrix of vessel conductances where l_j, d_j and μ_j denote the length, diameter and effective viscosity of segment j, respectively.

We used empirical *in vivo* blood viscosity laws, which prescribe the effective viscosity as a function of vessel diameter and haematocrit, to compute μ_j and consequently incorporate non-Newtonian effects in each individual microvessel[20]. Network haematocrit heterogeneity plays an important part in network flow resistance; however, access to data on haematocrit distributions is limited. In the absence of these data, empirical descriptions can be incorporated to include red blood cell screening, the process by which the balance of fluid forces determines a blood cell's destination[42]. The approach requires an iterative procedure in which flow Q_j in vessel j is used to update haematocrit, H_{Dj} in each vessel. Here, boundary haematocrit was assigned as 0.45 and the process was repeated until the sequence converges to given tolerances (10^{-3}) for both flow and haematocrit.

In the absence of measured flow data, the ill-posed system, (1), requires further assumptions to obtain a unique solution. The method proposed by Fry *et al.*[21] sought to solve a constrained optimisation problem, formulated in terms of a Lagrangian objective function that is defined by

$$\begin{aligned} L \;=\; & \frac{1}{2} k_p \sum_{k\in N} w_k (p_k - p_{0k})^2 + \frac{1}{2} k_\tau \sum_{j\in S} \ell_j (\tau_j - \tau_{0j})^2 \\ & + \sum_{i\in I\bigcup B} \lambda_i \left(\sum_{k\in N} K_{ik} p_k + Q_{0i} \right), \end{aligned} \tag{5}$$

where p_{0k} is the target pressure at node k, τ_j is the wall shear stress in segment j, τ_{0j} is the corresponding target shear stress, k_p and k_τ are weighting factors associated with the pressure and shear deviations from the target values, λ_i is the Lagrange multiplier associated with node i and w_k is the vessel length associated with node k. Setting $dL/dp_i = 0$ and combing with equation equations (1) yields the following sparse linear system

$$\begin{bmatrix} \mathbf{K} & 0 \\ k_\tau \mathbf{H} + k_p \mathbf{W} & \mathbf{K}^\mathbf{T} \end{bmatrix} \times \begin{bmatrix} \mathbf{P} \\ \lambda \end{bmatrix} = \begin{bmatrix} -\mathbf{Q_0} \\ k_p \mathbf{W} \times \mathbf{p_0} + k_\tau \mathbf{M}^\mathbf{T} \times (\boldsymbol{t_0} \cdot \mathbf{c} \cdot \ell) \end{bmatrix} \tag{6}$$

where $\mathbf{K}$, $\mathbf{W}$, $\mathbf{M}$ and $\mathbf{H}$, denote the matrix forms of K_{ik}, w_k, M_{ij} and H_{ik}, respectively. Note, $\mathbf{W}$ is a diagonal matrix with entries w_k and H_{ik} are defined as

$$w_j = \frac{1}{2}\sum \ell_j \quad \text{and} \quad H_{ik} = \sum_{j\in S} c_j^2 M_{ji} M_{jk} l_j, \tag{7}$$

where $c_j = 4\mu_j/(\pi r_j^3)$. The remaining variables $\mathbf{p}$, $\boldsymbol{\lambda}$, $\mathbf{Q_0}$, $\mathbf{p_0}$, $\boldsymbol{\tau_0}$, $\mathbf{c}$ and ℓ are the vector forms of p_k, λ_k, Q_{0i}, p_{0k}, τ_{0j}, c_j and ℓ_j respectively. The resulting sparse square linear system, (6), contains $n_I + n_B + n_N$ linear equations, where n_I, n_B and n_N are the number of interior, known boundary and the total number of nodes. We solved this system for unknowns p_i and λ_i using standard numerical methods.

Mathematical Oxygen Transport Model. We used our flow solutions from the discrete-network model to parametrise the following well-established approach which describes steady-state intravascular and tissue

oxygen transport, where by tissue is represented as a homogeneous medium with oxygen diffusivity D and solubility α, as outlined in a series of papers[19,43,44]. Derived from Fick's Law, tissue PO_2, P, conservation satisfies

$$D\alpha\nabla^2 P = M(P), \tag{8}$$

where $M(P)$ is the oxygen consumption rate. The dependence of oxygen consumption on PO_2 is represented by a Michaelis-Menten relationship

$$M(P) = \frac{M_0 P}{P_0 + P}, \tag{9}$$

where M_0 is a uniform oxygen demand in the tissue given a non-limiting supply of oxygen and P_0 represents the PO_2 at half-maximal consumption.

The rate of convective oxygen transport along a vessel segment is given by

$$f(P_b) = Q\left[H_D C_0 S(P_b) + \alpha_{eff} P_b\right], \tag{10}$$

where P_b is the blood PO_2 level, Q is the blood flow rate, H_D is the discharge haematocrit, C_0 is the concentration of haemoglobin-bound oxygen in a fully saturated erythrocyte, S is the oxyhemoglobin saturation and α_{eff} is the effective solubility of oxygen in blood. The Hill equation presents a simple description of oxyhemoglobin saturation, as a consequence of oxygen binding to hemoglobin, and is given by

$$S(P_b) = \frac{P_b^n}{P_b^n + P_{50}^n}, \tag{11}$$

where n is the Hill exponent and P_{50} is the PO_2 at 50% saturation. The effective solubility of oxygen in blood is given by

$$\alpha_{eff} = (1 - H_D)\alpha_p + H_D\alpha_{RBC}, \tag{12}$$

where α_p and α_{RBC} are the solubilities in blood plasma and in RBCs, respectively. These values are similar[45] implying haematocrit has a small weighting towards α_{eff}. Thus, allowing us to approximate the effective oxygen solubility by a constant value.

Conservation of oxygen flux infers

$$\frac{df(P_b)}{ds} = -q_v(s) \tag{13}$$

in each vessel segment, where s defines segment length and q_v is the rate of diffusive oxygen efflux per unit of s.

Continuity of oxygen flux and PO_2 (under the assumption of cylindrical vessel segments) across the vessel walls yields

$$q_v(s) = -D\alpha \int_0^{2\pi} \frac{\partial P}{\partial r} r_v d\theta, \tag{14}$$

where r_v is the vessel radius and integration is performed over the circumference of the vessel, denoted by the azimuthal angle θ. The blood vessel delivering the oxygen generally exceeds local PO_2 levels at the interface with the surrounding tissue. Hellums[46] defined the following jump condition at the interface

$$P_v(s) = P_b(s) - Kq_v(s), \tag{15}$$

where $P_v(s)$ is the average tissue PO_2 and K represents intravascular resistance to radial oxygen transport.

The oxygen transport model given by (8)-(15) is solved numerically[47] by formulating it in terms of Green's functions, following the established approach reported in Secomb *et al.*[19], whereby blood vessels are represented as a set of discrete oxygen sources. Using superposition principles, the resulting fields from these sources represent the PO_2 field in the tissue. If the rate of oxygen uptake within the tissue is prescribed, the only unknowns in the problem are the strengths of both the sources and sinks. We apply this mathematical model to our cortical microvascular network.

Modelling oxygen transport, the Green's function, $G(\mathbf{x}; \mathbf{x}')$, for a given tissue domain may be defined as the PO_2 at a point $\mathbf{x}$ resulting from a unit point source at $\mathbf{x}'$, through

$$D\alpha\nabla^2 G = -\delta_3(\mathbf{x} - \mathbf{x}'), \tag{16}$$

where D is oxygen diffusivity, α is oxygen solubility and δ_3 is the delta function in three-dimensions. Solving the adjoint problem the PO_2 is thus given by

$$P(\mathbf{x}) = \int_{Sources} G(\mathbf{x}; \mathbf{x}')q(\mathbf{x}')d\mathbf{x}', \tag{17}$$

where $q(\mathrm{x})$ represents the distribution of source strengths.

The oxygen field resulting from a blood vessel can be represented by a series of sources down its centre. Following the approach of Hsu & Secomb[44], the oxygen sources are located along the vessel axis and uniformly

distributed around the circumference of the vessel on the blood-tissue boundary. Whilst the approach uses an iterative scheme to incorporate the non-linear reaction rate kinetics, resolving the spatial oxygen fields for complex microvascular networks comes at a relatively low cost when compared to finite-difference methods alongside minimising artefacts associated with assigning BCs[19,44]. The numerical implementation of the Green's model is outlined in Secomb *et al.*[19]. In addition, a recent extension incorporates time-dependent solute transport[48].

Boundary Conditions and Parameter Assignment. Sensitivity analysis equivalent to that investigated by Fry *et al.*[21] estimation model on the mesenteric networks of Pries *et al.*[34] was replicated. Increasing the number of applied BCs reduced the normalised root mean square deviation between segment flows predicted with partial boundary information and those simulated when all BCs (Q_{0j}) are known. As network boundary pressure and flow data were unavailable for our cortical network, we extrapolated a function to compute arteriolar or venular pressures based on the vessel diameters using data from previous intra-cortical blood flow simulations by Lorthois *et al.*[6,7]. Lorthois *et al.*[6] a simulated a steep pressure drop on the arteriolar side compared to venules (a drop of 75 to 15 mmHg, with a mean capillary pressure of 31 mmHg), an asymmetry consistent with previous experimental studies Pries[39,49]. A function was fitted to this data in order to apply pressure conditions to the boundaries of our pial arteriolar and venula vessels (representing 2.3% of all BCs in the network - see Supplementary Fig. S5), using vessel classifications shown in Fig. 1c. In the absence of measured data, we applied a haematocrit of 0.45 at all boundary nodes (see Supplementary Fig. S4).

In the network flow estimation scheme, we assumed the target pressures at each node and target shear stresses in each segment to be constants (equal in magnitude for all segments). Target pressure, p_{0j}, assigned as the mean capillary pressure computed by Lorthois *et al.*[6], 31 mmHg. The sign of the shear stress, τ_{0j}, in each segment is equal to the corresponding flow sign, but this cannot be known until we obtain a solution. The target shear stresses (initially set with random flow signs and to a value of 5 dyn/cm^2) are used to estimate the flow distribution and then updated in each segment for the next iterative step, whilst updating the value of τ_{0j} to the mean vessel target wall shear stress on the previous iteration. During optimisation (with application to the rat mesentery networks of Pries *et al.*[34]), Fry *et al.*[21] initially set $k_\tau = 10^{-4}$ and on each iteration the value of k_τ was doubled until two consecutive iterations gave the same flow directions in all segments. The constant k_p is used to maintain pressures in a physiologically-realistic range (tested against the measured flows in the mesenteric networks[21]) and was arbitrarily set to 0.1 in order to bias the nodal pressures towards the specified target pressure. We employed an identical approach in this study.

When simulating constriction propagation of vessels, we used baseline capillary boundary pressures as BCs. Here, pressure was assumed to be maintained by adjoining tissue blocks. Similarly, the arteriolar and venular baseline flow solutions were used as BCs, with the exception that the base of the local penetrating arteriole was set as an unknown BC. We explored a variety of BC assignment in order to produce the required physiological velocity changes, in addition to network response. For example, inspired by observations of venular distension in response to arteriolar dilation[33], we investigated venular compression to match blood velocity changes to constriction, compared to those *in vivo*.

Simultaneous BCs for oxygen transport cannot be determined from available experimental information. In the Green's function method, the tissue volume is considered as being embedded in an infinite domain with the same diffusivity, where no oxygen sources or sinks are located externally to the given tissue region. Hence, we formed a well-posed problem without imposing explicit BCs on the outer surface of the tissue region. The method itself is parametrised by the discrete-network model, by inputting the computed flow and haematocrit values for each vessel segment. Alongside this, the model requires us to assign boundary PO_2 for network inlets, which can be a combination of arterioles, capillaries and venules. Based on experimental and simulated data, we assigned arterioles and venules PO_2 values of 90 and 40 mmHg, respectively[12]. In order to assign heterogenous capillary PO_2, we formed a data-fitted curve by extrapolating experimental data[22] in which PO_2 was measured relative to cortical depth (see Supplementary Fig. S6). The model's intravascular and tissue oxygen transport parameter values are given in Supplementary Table S2. Compared to previous cortical oxygenation studies[19], we assigned the consumption parameter, M_0, based on a recent study of $CMRO_2$ estimation (mean value of 1.71 μmol cm^{-3} min^{-1} used[32]). In this study, the Krogh cylinder model was applied, whilst taking into account that the rate of oxygen consumption is approximately 80–85% of its maximum value[50,51].

Data availability. Data are available upon request.

References

1. Dore, S. E. On the contractility and nervous supply of the capillaries. *British Journal of Dermatology* **35**, 398–404 (1923).
2. Hall, C. N. *et al.* Capillary pericytes regulate cerebral blood flow in health and disease. *Nature* **508**, 55–60 (2014).
3. Hamilton, N. B., Attwell, D. & Hall, C. N. Pericyte-mediated regulation of capillary diameter: a component of neurovascular coupling in health and disease. *Frontiers in neuroenergetics* **2**, 1–14 (2010).
4. Stefanovic, B. *et al.* Functional reactivity of cerebral capillaries. *Journal of Cerebral Blood Flow & Metabolism* **28**, 961–972 (2008).
5. Armulik, A., Genové, G. & Betsholtz, C. Pericytes: Developmental, Physiological, and Pathological Perspectives, Problems, and Promises. *Developmental Cell* **21**, 193–215 (2011).
6. Lorthois, S., Cassot, F. & Lauwers, F. Simulation study of brain blood flow regulation by intra-cortical arterioles in an anatomically accurate large human vascular network. Part II: Flow variations induced by global or localized modifications of arteriolar diameters. *NeuroImage* **54**, 2840–2853 (2011).
7. Lorthois, S., Cassot, F. & Lauwers, F. Simulation study of brain blood flow regulation by intra-cortical arterioles in an anatomically accurate large human vascular network: Part I: Methodology and baseline flow. *NeuroImage* **54**, 1031–1042 (2011).
8. Reichold, J. *et al.* Vascular graph model to simulate the cerebral blood flow in realistic vascular networks. *Journal of cerebral blood flow and metabolism: official journal of the International Society of Cerebral Blood Flow and Metabolism* **29**, 1429–1443 (2009).
9. Guibert, R., Fonta, C. & Plouraboué, F. Cerebral blood flow modeling in primate cortex. *Journal of cerebral blood flow and metabolism: official journal of the International Society of Cerebral Blood Flow and Metabolism* **30**, 1860–1873 (2010).

10. Gould, I. G., Tsai, P., Kleinfeld, D. & Linninger, A. The capillary bed offers the largest hemodynamic resistance to the cortical blood supply. *Journal of cerebral blood flow and metabolism: official journal of the International Society of Cerebral Blood Flow and Metabolism* **37**, 52–68 (2017).
11. Gagnon, L. *et al*. Multimodal reconstruction of microvascular-flow distributions using combined twophoton microscopy and Doppler optical coherence tomography. *Neurophotonics* **2**, 015008 (2015).
12. Gagnon, L. *et al*. Quantifying the microvascular origin of BOLD-fMRI from first principles with twophoton microscopy and an oxygen-sensitive nanoprobe. *The Journal of neuroscience: the official journal of the Society for Neuroscience* **35**, 3663–75 (2015).
13. Hill, R. A. *et al*. Regional blood flow in the normal and ischemic brain Is controlled by arteriolar smooth muscle cell contractility and not by capillary pericytes. *Neuron* **87**, 95–110 (2015).
14. Fernández-Klett, F., Offenhauser, N., Dirnagl, U., Priller, J. & Lindauer, U. Pericytes in capillaries are contractile *in vivo*, but arterioles mediate functional hyperemia in the mouse brain. *Proceedings of the National Academy of Sciences of the United States of America* **107**, 22290–22295 (2010).
15. Wei, H. S. *et al*. Erythrocytes Are Oxygen-Sensing Regulators of the Cerebral Microcirculation. *Neuron* **91**, 851–862 (2016).
16. Kisler, K. *et al*. Pericyte degeneration leads to neurovascular uncoupling and limits oxygen supply to brain. *Nature Neuroscience*, 406–416 (2017).
17. Armstrong, J. J., Larina, I. V., Dickinson, M. E., Zimmer, W. E. & Hirschi, K. K. Characterization of bacterial artificial chromosome transgenic mice expressing mCherry fluorescent protein substituted for the murine smooth muscle α-actin gene. *Genesis* **48**, 457–463 (2010).
18. Sanderson, C. & Curtin, R. Armadillo: a template-based C++ library for linear algebra. *Journal of Open Source Software* **1**, 26 (2016).
19. Secomb, T. W., Hsu, R., Park, E. Y. H. & Dewhirst, M. W. Green's Function Methods for Analysis of Oxygen Delivery to Tissue by Microvascular Networks. *Annals of biomedical engineering* **32**, 1519–1529 (2004).
20. Pries, A. R. & Secomb, T. W. Microvascular blood viscosity *in vivo* and the endothelial surface layer. *American journal of physiology. Heart and circulatory physiology* **289**, H2657–H2664 (2005).
21. Fry, B. C., Lee, J., Smith, N. P. & Secomb, T. W. Estimation of Blood Flow Rates in Large Microvascular Networks. *Microcirculation* **19**, 530–538 (2012).
22. Sakadžić, S. *et al*. Large arteriolar component of oxygen delivery implies a safe margin of oxygen supply to cerebral tissue. *Nature Communications* **5**, 5734 (2014).
23. Maeda, K., Mies, G., Oláh, L. & Hossmann, K. A. Quantitative measurement of local cerebral blood flow in the anesthetized mouse using intraperitoneal [14C]iodoantipyrine injection and final arterial heart blood sampling. *Journal of cerebral blood flow and metabolism: official journal of the International Society of Cerebral Blood Flow and Metabolism* **20**, 10–4 (2000).
24. Xu, K. *et al*. In Oxygen Transport to Tissue XXXII 255–260 (Springer US, 2011). https://doi.org/10.1007/978-14419-7756-4_34.
25. Chen, B. R., Kozberg, M. G., Bouchard, M. B., Shaik, M. A. & Hillman, E. M. C. A critical role for the vascular endothelium in functional neurovascular coupling in the brain. *Journal of the American Heart Association* **3** (2014).
26. Hartmann, D. A. *et al*. Pericyte structure and distribution in the cerebral cortex revealed by highresolution imaging of transgenic mice. *Neurophotonics* **2**, 041402 (2015).
27. Schmid, F., Reichold, J., Weber, B. & Jenny, P. The impact of capillary dilation on the distribution of red blood cells in artificial networks. *American Journal of Physiology -Heart and Circulatory Physiology* **308**, H733–H742 (2015).
28. Lücker, A., Secomb, T. W., Weber, B. & Jenny, P. The relative influence of hematocrit and red blood cell velocity on oxygen transport from capillaries to tissue. *Microcirculation* **24**, e12337 (2017).
29. Pries, A. R. *et al*. Resistance to blood flow in microvessels *in vivo*. *Circulation research* **75**, 904–915 (1994).
30. Fry, B. C., Roy, T. K. & Secomb, T. W. Capillary recruitment in a theoretical model for blood flow regulation in heterogeneous microvessel networks. *Physiological Reports* **1** (2013).
31. Secomb, T. W., Hsu, R., Beamer, N. B. & Coull, B. M. Theoretical simulation of oxygen transport to brain by networks of microvessels: effects of oxygen supply and demand on tissue hypoxia. *Microcirculation* **7**, 237–247 (2000).
32. Sakadžic, S. *et al*. Two-photon microscopy measurement of cerebral metabolic rate of oxygen using periarteriolar oxygen concentration gradients. *Neurophotonics* **3**, 045005 (2016).
33. Drew, P. J., Shih, A. Y. & Kleinfeld, D. Fluctuating and sensory-induced vasodynamics in rodent cortex extend arteriole capacity. *Proceedings of the National Academy of Sciences of the United States of America* **108**, 8473–8 (2011).
34. Pries, A. R., Ley, K. & Gaehtgens, P. Generalization of the Fahraeus principle for microvessel networks. *The American journal of physiology* **251**, H1324–32 (1986).
35. Dietrich, H. H., Kajita, Y. & Dacey, R. G. Local and conducted vasomotor responses in isolated rat cerebral arterioles. *The American journal of physiology* **271**, H1109–16 (1996).
36. Duvernoy, H. M., Delon, S. & Vannson, J. L. Cortical blood vessels of the human brain. *Brain Research Bulletin* **7**, 519–578 (1981).
37. Ren, H. *et al*. Cocaine-induced cortical microischemia in the rodent brain: clinical implications. *Molecular Psychiatry* **17**, 1017–1025 (2012).
38. Schindelin, J. *et al*. Fiji: an open-source platform for biological-image analysis. *Nature Methods* **9**, 676–682 (2012).
39. Pries, A. R., Secomb, T. W., Gaehtgens, P. & Gross, J. F. Blood flow in microvascular networks. *Experiments and simulation. Circulation Research* **67**, 826–834 (1990).
40. Pries, A. R. & Secomb, T. W. In Microcirculation 3–36 (John Wiley & Sons, Inc., Hoboken, NJ, USA, 2011).
41. Pries, A. R., Secomb, T. W. & Gaehtgens, P. Structure and hemodynamics of microvascular networks: heterogeneity and correlations. *The American journal of physiology* **269**, H1713–22 (1995).
42. Pries, A. R., Ley, K., Claassen, M. & Gaehtgens, P. Red cell distribution at microvascular bifurcations. *Microvascular research* **38**, 81–101 (1989).
43. Gagnon, L. *et al*. Modeling of Cerebral Oxygen Transport Based on *In vivo* Microscopic Imaging of Microvascular Network Structure, Blood Flow, and Oxygenation. *Frontiers in Computational Neuroscience* **10**, 82 (2016).
44. Hsu, R. & Secomb, T. W. A Green's function method for analysis of oxygen delivery to tissue by microvascular networks. *Mathematical Biosciences* **96**, 61–78 (1989).
45. Hellums, J. D., Nair, P. K., Huang, N. S. & Ohshima, N. Simulation of intraluminal gas transport processes in the microcirculation. *Annals of Biomedical Engineering* **24**, 1–24 (1995).
46. Hellums, J. D. The resistance to oxygen transport in the capillaries relative to that in the surrounding tissue. *Microvascular research* **13**, 131–6 (1977).
47. Secomb, T. W. Green's function method for simulation of oxygen transport to tissue http://physiology. arizona.edu/people/secomb/greens (2011).
48. Secomb, T. W. A Green's function method for simulation of time-dependent solute transport and reaction in realistic microvascular geometries. *Mathematical medicine and biology: a journal of the IMA*, **031** (2015).
49. Lipowsky, H. H. Microvascular rheology and hemodynamics. *Microcirculation* **12**, 5–15 (2005).
50. Angleys, H., Østergaard, L. & Jespersen, S. N. The effects of capillary transit time heterogeneity (CTH) on brain oxygenation. *Journal of cerebral blood flow and metabolism: official journal of the International Society of Cerebral Blood Flow and Metabolism* **35**, 806–17 (2015).
51. Gjedde, A., Johannsen, P., Cold, G. E. & Ostergaard, L. Cerebral metabolic response to low blood flow: possible role of cytochrome oxidase inhibition. *Journal of cerebral blood flow and metabolism: official journal of the International Society of Cerebral Blood Flow and Metabolism* **25**, 1183–96 (2005).

Acknowledgements
We would like to thank R.A. Hill and J. Gruztendler for acquiring and supplying the imaging data. In addition, Seyyed Haqshenas and Iva Burova for discussions into the oxygen transport model parameter assignment. This study was supported by EPSRC (EP/L504889/1), Rosetrees Trust (M601) and NIH (RO1 NS089734).

Author Contributions
All authors were involved in the design of the study. S.W.S. processed and segmented the image data. P.W.S. performed numerical simulations. All authors contributed to the writing of the manuscript.

Additional Information
Supplementary information accompanies this paper at https://doi.org/10.1038/s41598-017-19086-z.

Competing Interests: The authors declare that they have no competing interests.

Publisher's note: Springer Nature remains neutral with regard to jurisdictional claims in published maps and institutional affiliations.